Surface-phonon dispersion curves of TiC(100)

C. Oshima, T. Aizawa, M. Wuttig,* R. Souda, S. Otani, and Y. Ishizawa
National Institute for Research in Inorganic Materials, 1-1 Namiki, Sakura-mura, Niihari-gun, Ibaraki-ken 305, Japan

H. Ishida and K. Terakura
The Institute for Solid State Physics, The University of Tokyo, 7-22-1 Roppongi, Minato-ku, Tokyo 106, Japan
(Received 27 May 1987)

The surface-phonon dispersion curves of the TiC(100) surface along both the $\bar{\Gamma}\bar{M}$ and $\bar{\Gamma}\bar{X}$ azimuths of the two-dimensional Brillouin zone have been measured by electron-energy-loss spectroscopy (EELS). We have observed two acoustical-phonon branches (Rayleigh and resonance modes) and three optical-phonon branches (Wallis, Lucas, and new modes). Those experimental curves are in good agreement with the theoretical ones calculated on the basis of a screened-shell model. In this calculation, the 20% stiffening of the stretching force constant between the first-layer Ti atom and the second-layer carbon produces a quasitransverse mode localized strongly at the second-layer carbon, which corresponds to the new observed surface mode. The local spectral densities calculated with use of these parameters have been compared with the experimental EELS spectra.

I. INTRODUCTION

Because of the simple atomic configuration, a (100) surface of a rock-salt-structured crystal has provided a good testing field for understanding microscopic surface phonons for a long time. They have been studied theoretically by a number of authors. In 1957, Wallis discussed an edge-localized mode of a diatomic linear chain (one-dimensional model),[1] and then Wallis, Mills, and Maradudin found a similar surface-localized optical mode with a vibration perpendicular to the surface ("Wallis mode") on the NaCl(100) surface (three-dimensional model) in 1968.[2] In the same year, independently, Lucas found another surface optical mode associated with vibration parallel to the surface ("Lucas mode").[3] These microscopic surface modes are strongly localized at a few atomic layers near the surface. Subsequently, Tong and Maradudin carried out a calculation of optical and acoustical surface phonons throughout the two-dimensional Brillouin zone of the NaCl(100) surface.[4] In the 1970s, Chen, Alldrege, deWette, and Allen calculated the surface phonons of the (100) surface of some alkali halides in detail.[5] For metallic superconducting compounds, recently, the surface phonons of TiN(100), TaC(100) and NbC(100) were discussed.[6,7] While all these calculations were performed for the ideal surface without surface relaxation, in the past few years surface-phonon dispersion curves were calculated by considering the surface relaxation.[8,9]

In contrast to these theoretical efforts, a few experimental works on this subject have been done. The dispersion curves of Rayleigh mode started to be measured in 1980 by inelastic He scattering,[10] but the microscopic optical modes were detected only in 1984 by using electron-energy-loss spectroscopy (EELS). The Wallis mode was first measured by the present authors on the TaC(100) surface,[11] and subsequently, various modes have been observed on the (100) surface of various transition-metal carbides.[12–14] Independently, both modes (Wallis and Lucas) on NaF(100) were observed by Brusdeylins *et al.* using inelastic He scattering.[15]

Recently, we reported preliminary results about the surface phonons on the TiC(100) surface.[14] The observed surface-phonon dispersion curves along the $\bar{\Gamma}\bar{M}$ azimuth have been assigned on the basis of the calculation including only a short-range force. But this calculation does not have enough accuracy for describing the observed dispersion curves, because TiC has complex chemical bonds including both ionic and metallic character. In this paper, therefore, we have tried to explain the surface-phonon dispersion curves along both the $\bar{\Gamma}\bar{X}$ and $\bar{\Gamma}\bar{M}$ azimuths by using a screened shell model, which has successfully explained the dispersion curves of the bulk phonons.[16] The experimental conditions such as apparatus and sample preparation are described in the next section, and the experimental results are exhibited in Sec. III. These data are compared with the theoretical ones in Sec. IV, and the nature of the phonon structure near the (100) surface is discussed.

II. EXPERIMENT

The $TiC_{0.96}$ specimens used in this experiment were cut from large single crystals, which were grown by the zone-melting method. One face was polished mechanically to an optical flat. The surface was finally cleaned by repeated heatings up to 1600 °C under an ultra high-vacuum condition. After those procedures, the (100) surface showed sharp low-energy-electron diffraction (LEED) spots corresponding to a 1×1 atomic structure, and no contaminations were detected by Auger-electron spectroscopy (AES) and EELS.[17] Additionally, impact-collision ion scattering spectroscopy (ICISS) showed that the carbon vacancies on the TiC surface disappeared

with the repeated heatings,[18] which is crucial information for the phonon properties because the bulk phonons of the transition-metal carbides are largely changed by changing the carbon-vacancy density in bulk.[19] An EELS spectrometer is composed of a tandem monochromator and a tandem analyzer. The energy resolution of ~ 4 meV was obtained routinely at the sample current of $\sim 10^{-10}$ A. The direct current measured at an entrance position of a channeltron was $\sim 8\times 10^{-12}$ A under the energy resolution of ~ 4 meV. The incident angle of the impinging beam was rotated around the specimen in order to change the wave vector of the excited surface phonon. Figures 1(a) and 1(b) show the two-dimensional TiC(100) lattice and the corresponding two-dimensional Brillouin zone, respectively. For the measurement of the dispersion curves along the $\bar{\Gamma}\bar{M}$ azimuth, the monochromatized beam was rotated along the [010] azimuth, while the analyzer was fixed in the polar direction 18° from the surface horizontal as shown in Fig. 2. The angle change in the incident beam, $\Delta\theta$, was measured from the specular direction (Fig. 2). Typical measuring periods for one EELS spectrum were 5–20 min, depending on the signal intensity. The loss energies of the scattered electrons were measured, and at the same time, the wave vectors of the excited phonons were calculated from the conservation law of the momentum parallel to the surface. Namely,

$$\mathbf{K}_{S,\parallel}-\mathbf{K}_{I,\parallel}=\mathbf{q}_{\parallel}-\mathbf{G}_{\parallel}\ . \tag{1}$$

Here, the vectors $\mathbf{K}_{s,\parallel}$ and $\mathbf{K}_{I,\parallel}$ are the wave vectors of the scattered electrons and the incident electrons, respectively. The symbol $\parallel$ stands for the component parallel to the surface. The wave vectors of the surface phonon and the reciprocal vector are denoted by $\mathbf{q}$ and $\mathbf{G}$, respectively. Our system was additionally equipped with a cylindrical mirror analyzer for Auger analysis, and a LEED screen in the same chamber, which was evacuated to less than 1×10^{-8} Pa.

III. EXPERIMENTAL RESULTS

Figure 3 shows the typical specular EELS spectra for a clean surface [Fig. 3(a)] and for a surface after a one-day lapse under ultrahigh vacuum [Fig. 3(b)]. The TiC(100) surface is fairly inert for gas chemisorption compared to the active surfaces such as Ti(0001) and TiC(111).[17] At room temperature, for instance, no hydrogen (H_2) gas is chemisorbed on the TiC(100) face, and the sticking coefficient of oxygen gas on the (100) surface is 2 orders of magnitude smaller than that for the Ti(0001) surface.[17] As shown in Fig. 3(b), two loss peaks, the characteristic feature of the clean (100) surface, can be observed after a one-day lapse, which is considerably different from the other carbide surfaces; on the HfC(100) and ZrC(100) surfaces, these peaks disappeared completely after a few hours lapse under the same vacuum condition.

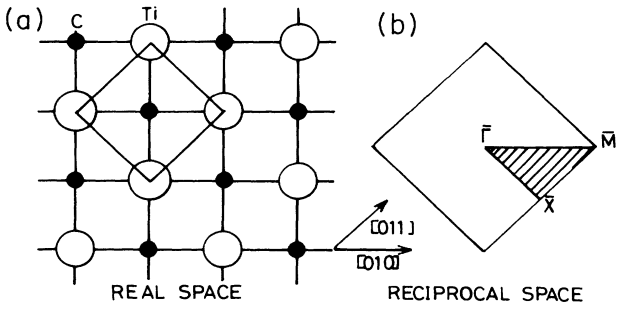

FIG. 1. Two-dimensional lattice of the TiC(100) surface (a) and the corresponding Brillouin zone (b). The shaded triangle in (b) is the irreducible portion of the first Brillouin zone.

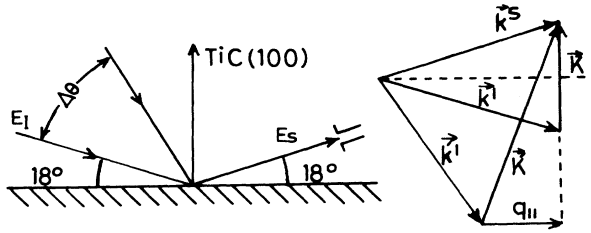

FIG. 2. Schematic diagram of the scattering geometry in this experiment. The energy analyzer was fixed at a certain polar angle, while the monochromatic incident beam was rotated around the specimen. The wave vector $\mathbf{q}_{\parallel}$ of the excited surface phonon was determined from the momentum-conservation law.

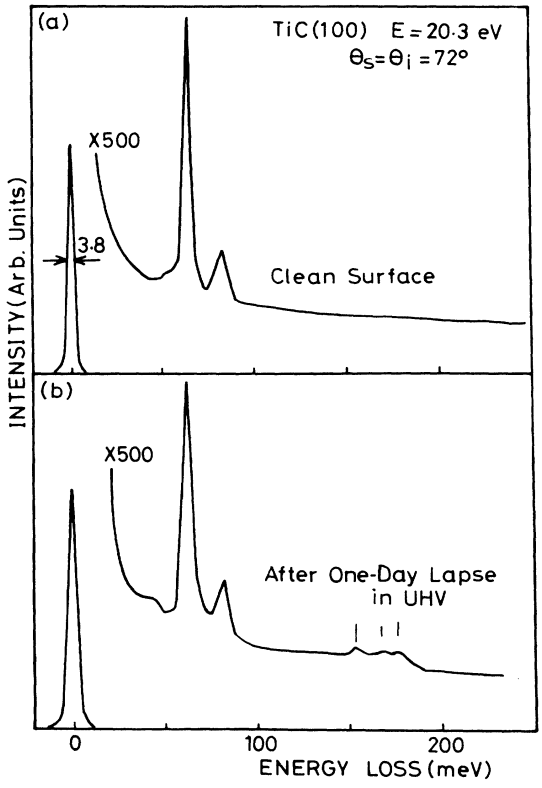

FIG. 3. Typical specular spectra. The clean surface (a) and the contaminated surface after a one-day lapse in UHV (b).

A sequence of angle-resolved EELS spectra of the clean surface is shown in Fig. 4. Each spectrum was measured within 5–20 min immediately after the flash heating for cleaning. Some losses denoted by S_1, S_2, S_2', S_4, and S_6 are observed. Both the loss energies and the intensities changed largely with changing the incident direction, $\Delta\theta$. The angular distribution of the S_2 and S_2' intensities possesses a dipole lobe around the specular direction as reported in a previous paper;[14] these peak intensities in the specular direction are about 2 orders of magnitude larger than those in the off-specular direction. The wave vector $\mathbf{q}_\parallel$ in Fig. 4 was determined from the conservation law of Eq. (1). The plots of the loss energy against $q_\parallel$ provide the energy dispersion curves. Figure 5 shows the dispersion curves along the $\bar{\Gamma}\bar{M}$ azimuth, while the corresponding data for the $\bar{X}$ azimuth are shown in Fig. 6. The data points obtained for different primary energies agreed with each other within the experimental accuracy of ± 1.5 meV. The surface phonon data are symmetric with respect to the zone boundary as can be seen in Fig. 6 around the $\bar{X}$ point. The solid and dotted curves in Figs. 5 and 6 are the theoretical ones, which will be discussed in detail in the next section.

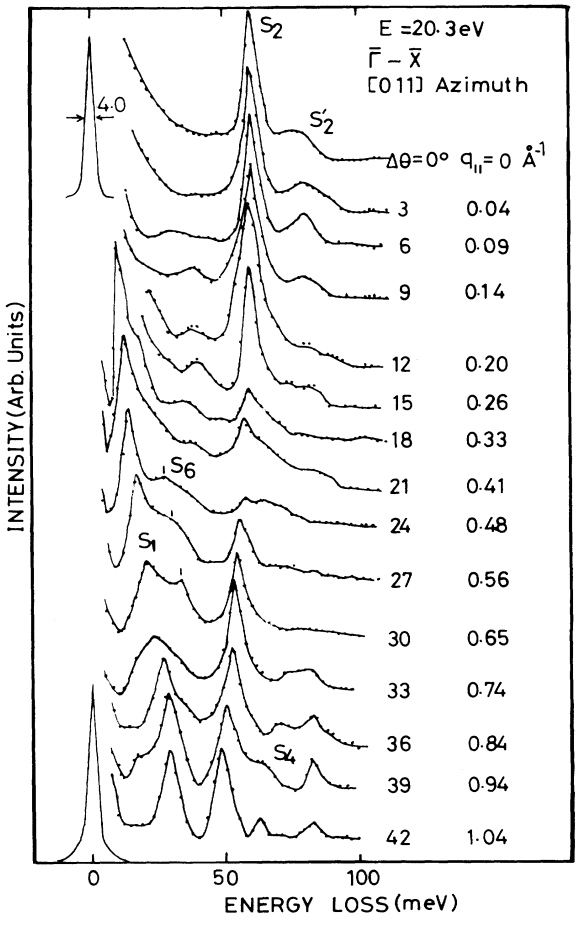

FIG. 4. Typical angle-resolved EELS spectra of the clean TiC(100) surface. The symbol $\Delta\theta$ is the angle change of incident beam measured from the specular direction.

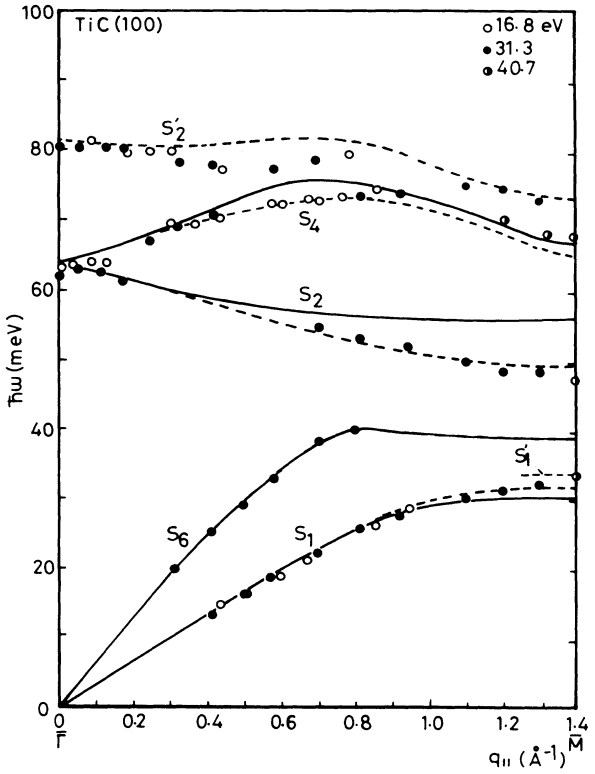

FIG. 5. Experimental plots in the irreducible portion of the Brillouin zone along the $\bar{\Gamma}\bar{M}$ azimuth. Theoretical dispersion curves are also drawn by the solid lines for the unrelaxed surface, and the dotted lines for the relaxed surface (see text).

IV. DISCUSSIONS

A. Dispersion-curve calculation based on a screened shell model

Because of the complex-bond character of the transition-metal carbides, a screened shell model is required to explain the dispersion curves of their bulk phonons. In this model, the following forces and effects are included: (1) the short-range force, (2) the long-range Coulomb force, (3) atomic polarization, and (4) screening of the Coulomb force by free electrons.

The bulk data of TiC are successfully explained with the screened shell model including 12 parameters.[16] Using the same model with the same bulk parameters, here we have calculated the surface and the bulk phonons in a slab-shaped TiC crystal with the (100) orientation. Similar slab calculations have been applied to various ionic compounds with a NaCl structure by Chen *et al.*,[5] and yielded successfully the interesting surface effects of the lattice vibration. The slab-shaped crystal used in this calculation consists of 16 atomic layers, which is thick enough to describe the microscopic surface phonons of the ionic crystals.[5] Concerning the screening effects of free electrons, we have used the formula in the "specular reflection approximation" derived by Ishida and Terakura.[7] The formulation is different from Weber's bulk formula,[20] and therefore two different parameters (screening length and charge) were adjusted to

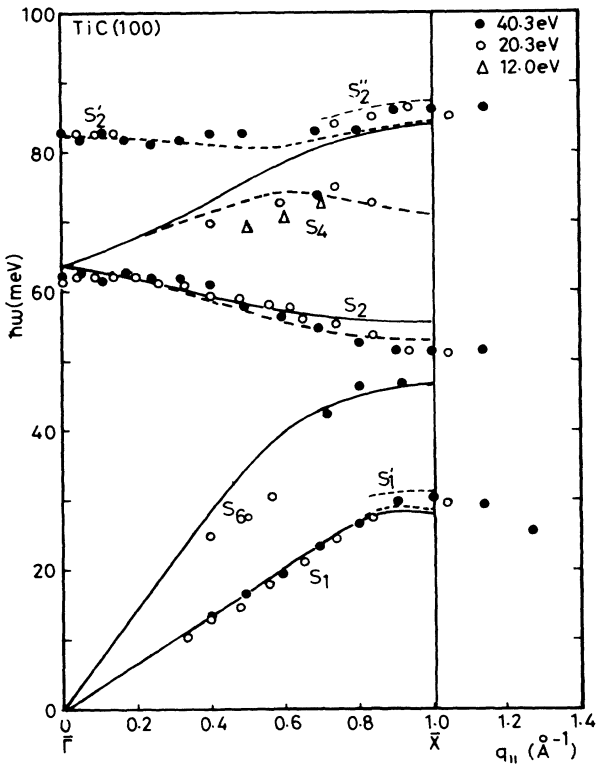

FIG. 6. Experimental plots in the irreducible portion of the Brillouin zone along the $\bar{\Gamma}\bar{M}$ azimuth. The solid and dotted curves are the theoretical ones from the unrelaxed and relaxed surfaces, respectively. The mirror symmetry plane can be observed at the $\bar{X}$ point.

provide the same surface-projected bulk continua as measured by neutron inelastic scattering. In this calculation, we assumed an ideal surface structure; i.e., no position change of the surface atoms from the ideal ones in the bulk, following the LEED and ISS experiments.[17,21]

Figures 7 and 8 show the theoretical results for an "unrelaxed surface" and a "relaxed surface," respectively. Here, unrelaxed surface means no change in the bulk parameters near the surface, which corresponds to the "ideal surface" without atomic and electronic relaxation. In the case of the relaxed surface, on the other hand, these parameters of the lattice dynamical calculation were adjusted near the surface in order to fit to the experimental curves. The hatched regions in these figures are the surface-projected bulk-phonon continua. The dispersion curves along the $\bar{\Gamma}\bar{X}$ and $\bar{\Gamma}\bar{M}$ azimuths of the two-dimensional Brillouin zone are shown. Owing to the mirror-plane symmetry in the $\bar{\Gamma}\bar{M}$ and $\bar{\Gamma}\bar{X}$ direction, vibrational modes are decoupled into the sagittal-plane (SP) modes and the shear-horizontal (SH) modes. Only the SP modes are observable in this experiment. The surface modes illustrated by solid curves in Figs. 7 and 8 are named in a way similar to Chen's notation.[5] Namely, there is the Rayleigh wave S_1, the quasi-longitudinal-acoustical (LA) mode S_6, the quasi-transverse-optical (TO) mode S_2 (Wallis mode), and the quasi-longitudinal-optical (LO) mode S_4 (sagittal Lucas mode). They are all SP modes. The unobservable SH

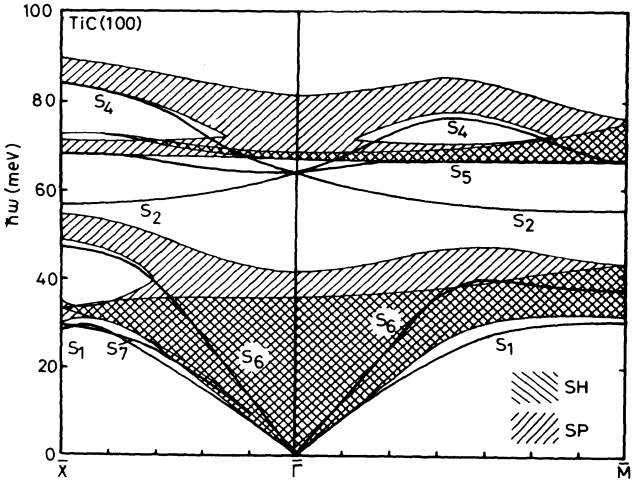

FIG. 7. Theoretical surface-phonon dispersion curves of the unrelaxed surface, which are calculated on the basis of a screened shell model with 12 parameters. The parameters used in this calculation were determined from the bulk-phonon experiment. The hatched regions are the bulk-phonon continua. The solid curves stand for the surface localized modes.

modes S_7 and S_5 (SH Lucas mode) also appear either just below or inside the bulk continuum.

The C_{4v} point-group symmetry requires the degeneracy of two Lucas modes (S_4 and S_5) at both the $\bar{\Gamma}$ and $\bar{M}$ points. For this surface, accidentally, the vibrational energy of Wallis mode S_2 coincides with those of the Lucas modes at the $\bar{\Gamma}$ point. We compared the surface phonons of the unrelaxed surface with the experimental data in Figs. 5 and 6. The solid curves indicate the calculated SP surface phonon modes.

They roughly agree with some of the observed modes (S_1, S_2, and S_6). Moreover, this result explains a feature of the observed S_6 loss intensities; in this experiment,

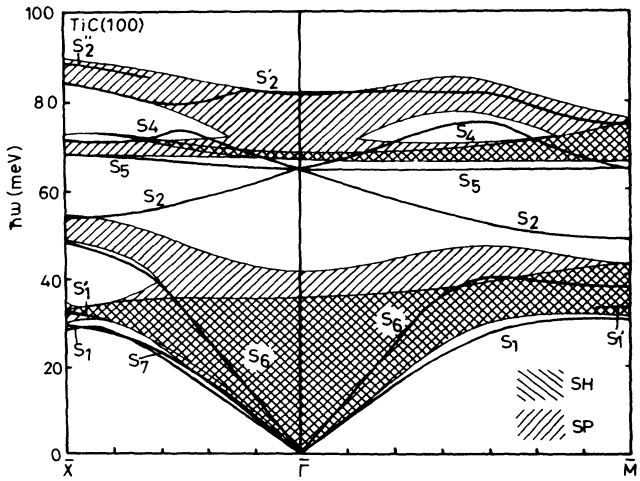

FIG. 8. The theoretical surface-phonon dispersion curves for the relaxed surface. Three short-range force constants near the surface are changed (see text). A new vibrational mode S_2' appears above the bulk continua, and it hybridizes with the S_4 (sagittal Lucas) mode halfway between the $\bar{\Gamma}$ and $\bar{X}$ points.

the S_6 mode can be observed near the $\bar{X}$ point, but not near the $\bar{M}$ point. As shown in Fig. 7, S_6 couples strongly with the bulk modes near the $\bar{M}$ point resulting in delocalization, while S_6 becomes a highly localized mode near the $\bar{X}$ point, because it is located in the gap inside the acoustical continuum.

Regarding S_1 and S_2, there are some differences between the experimental curves and the theoretical ones at the two zone boundaries $\bar{X}$ and $\bar{M}$, which will be discussed later. The main problem of the calculation for the unrelaxed surface is the failure to produce the observed S_2' mode, which means that we cannot explain the S_2' mode without surface relaxation. The observed vibrational energy of the S_2' mode at the $\bar{\Gamma}$ point is about 82 meV, which is higher than the maximum value of the bulk phonons. According to Rayleigh's theorem,[22] generally speaking, we cannot expect surface phonons above the bulk-phonon band without a stiffening of force constant.

Next, we summarize the vibrational properties of the S_2' mode.

(1) The angular distribution of the S_2' intensity shows a dipole lobe around the specular direction, a characteristic feature of dipole scattering. With this scattering mechanism, only totally symmetric modes can be observed. Since the atomic arrangement of the TiC(100) surface is invariant under all operators forming the symmetry group C_{4v}, the atomic displacement of the S_2' mode at the $\bar{\Gamma}$ point must belong to the total symmetric A_1 representation. Therefore, the polarization of the S_2' mode is purely perpendicular to the surface at the $\bar{\Gamma}$ point.[23]

(2) Let us consider only the vibration of the topmost layer at the $\bar{\Gamma}$ point. There are six modes corresponding to the freedom of two atoms in the surface unit cell. Three acoustical modes have zero vibrational energies. The remaining three modes are optical modes; they are two Lucas modes (E representation) and one Wallis mode (A_1 representation). We can expect only one observable mode (S_2) as the dipole active vibration within the freedom of the topmost layer. Hence, the S_2' mode should come from the freedom of the inner atomic layers such as the second and/or third layers.

(3) The high vibrational energy of S_2' indicates that the carbon vibration is dominant in this mode, which is also consistent with another experimental result; the same S_2' mode has been found at almost the same energy just above the bulk optical bands on the ZrC(100) and HfC(100) surfaces.[22,24,25]

The vibration of the second-layer carbon is the most plausible origin of the S_2' mode as compared with the deeper-layer carbon for the following reason. Concerning the nearest- and second-nearest-neighbor configuration, the second-layer carbon has the same arrangement as the bulk carbon. However, the short-range forces between the first and second layers are possibly modified by the electronic and/or atomic relaxation of the first layer. In order to explain the high energy of the S_2' mode, the stretching force constant between the first-layer Ti atom and the second-layer carbon is required to be stiffened. To confirm this conjecture, we calculated the surface-phonon dispersion curves of the relaxed surface, in which the surface parameters of the short-range forces were changed as shown in Table I. The essential aspects of this calculation are summarized as follows.

(1) The stretching force constant between the first-layer Ti atom and the second-layer carbon atom is stiffened by 20%. As we discussed above, it is necessary to explain the existence of the S_2' branch.

(2) The second-neighbor stretching force constant between the first- and second-layer Ti atoms is stiffened by 18%. This is necessary to increase the vibrational energy of the Rayleigh mode near the zone boundaries.

(3) The noncentral force constant $C(11)$ between the second-neighbor carbon atoms within the first layer was introduced for the reduction of the Wallis (S_2) energy at the zone boundaries. Its value amounts to 27% of the noncentral force constant $C(22)$ between the second-neighbor Ti atoms.

The results of the dispersion curves are shown in Fig. 8. The main difference between Figs. 7 and 8 is the appearance of the S_2' mode just above the bulk optical bands at the $\bar{\Gamma}$ point, and the S_2' mode shows monotonic downward dispersion up to the zone boundary $\bar{X}$, while the S_4 (sagittal Lucas) mode bends up from to $\bar{X}$. Those branches are hybridized at the middle of $\bar{\Gamma}\bar{X}$, and then

TABLE I. The short-range parameters of the shell model used to fit the observed dispersion curves. Force constants are given in units of $e^2/4r_0^3$. Here e is the electron charge and r_0 is the nearest-neighbor atomic distance. The other parameters used in this calculation are the same as the bulk values in Ref. 14. The symbol A and B (C) are central (noncentral) force constants, respectively. The numbers 1 and 2 in parentheses refer to carbon and metal atoms, respectively.

	In bulk	Intralayer force constants of the first layer	Interlayer force constants between the first and second layers
$A(12)$	25.72	25.72	25.72×1.20
$B(12)$	0.69	0.69	0.69
$A(11)$	0.0	0.0	0.0
$B(11)$	0.0	0.0	0.0
$C(11)$	0.0	−0.36	0.0
$A(22)$	8.58	8.58	8.58×1.18
$B(22)$	−3.29	−3.29	−3.29
$C(22)$	1.34	1.34	1.34

form new hybridized branches. In the $\bar{\Gamma}\bar{M}$ direction, on the other hand, the S_4 mode bends up in the initial half zone, and then goes down near the zone boundary; therefore there is no chance for a hybridization between the S_2' and S_4 modes.

These theoretical curves both for the unrelaxed (solid curves) and relaxed (dotted curves) surfaces are compared with the experimental ones in Figs. 5 and 6. The acoustical longitudinal mode S_6 is affected only marginally by the parameter changes described above. One can see that the results for the relaxed surface agree fairly well with the experimental ones. Two new branches of the relaxed surface near the zone boundaries, S_1' and S_2'', will be discussed in the next section.

B. Local spectral densities

By using the parameters determined above, we have calculated the local phonon-spectral density, defined as

$$\rho_{\alpha\beta}(l,\kappa;l',\kappa';\mathbf{q}_{\parallel},\omega) = \sum_s e_\alpha^s(\mathbf{q}_{\parallel};l,\kappa)e_\beta^{s*}(\mathbf{q}_{\parallel};l',\kappa')\delta(\omega-\omega^s(\mathbf{q}_{\parallel})) , \quad (2)$$

where $e_\alpha^s(\mathbf{q}_{\parallel};l,\kappa)$ is the α component of the eigenvector of mode S at atom κ in layer l. The symbol $\mathbf{q}_{\parallel}$ stands for the parallel component of the wave vector, and its eigenfrequency is $\omega^s(\mathbf{q}_{\parallel})$. For a slab calculation with finite number of eigenmodes, the δ function of $\rho_{\alpha\beta}$ in Eq. (2) was approximated by a Lorentzian with an energy width of 3.8 meV.

The local spectral densities calculated for the relaxed surface with the parameters in Table I are shown in Figs. 9–11. For comparison, the typical EELS spectra are also shown in the lower part of these figures. Figure 9 shows the spectral densities at the $\bar{\Gamma}$ point for the first-layer carbon [solid curve, $\rho_{zz}(1,\mathrm{C})$] and the second-layer carbon [dotted curve, $\rho_{zz}(2\mathrm{C})$]. Only the spectral densities of the polarization perpendicular to the surface (the z direction) are shown, because the observed peaks (S_2' and S_2) originate from the perpendicular vibrations as discussed above. These spectral densities show only weak mode mixing between the first- and second-layer carbons; namely, in the S_2 mode only the first-layer carbon vibrates and the vibration of the second-layer carbon can be neglected, and vice versa for the S_2' mode. The vibrational amplitudes of these modes are, therefore, strongly localized either at the first-layer carbon or at the second-layer carbon.

The observed EELS intensities of the two modes are significantly different from the calculated spectral density. There are the following possible origins for this discrepancy. Firstly, in the dipole scattering, generally speaking, the incident electrons are scattered outside the crystal by the dipole field, which flows out into the vacuum. The conduction electrons in bulk shield the dipole field, and this shielding affects strongly the dipole field generated at the second layer as compared with the field at the first layer. The damping factor was estimated to be about 0.33 by using the same parameter used in the phonon calculation, which is in rough agreement with

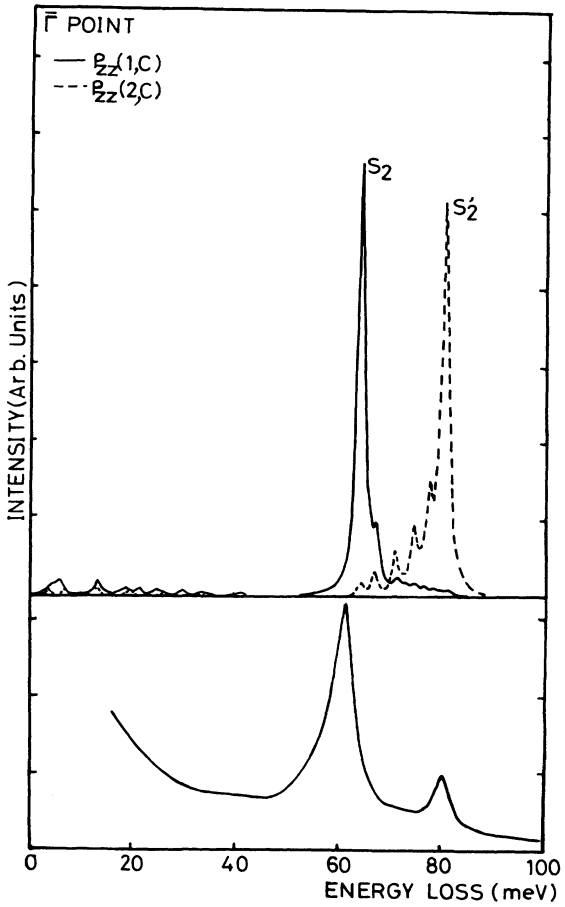

FIG. 9. Local spectral density of the relaxed surface (Fig. 8) at the Γ point ($\mathbf{q}_{11}=\mathbf{0}$) and the specular EELS spectrum (lower part). The spectral densities of the first- and second-layer carbon atoms in the perpendicular direction are shown, because only the perpendicular vibrations are observed by the dipole scattering in this case.

the intensity ratio of the S_2' peak to the S_2 peak (0.23 ± 0.05). This fact also supports our assignment that the origin of the S_2' mode is the perpendicular vibration of the second-layer carbon atoms. Secondly, the charge distribution around the carbon may be deformed at the first layer owing to the surface effect. Hence, the dynamical dipole moments of the first layer are possibly changed from the bulk value.

Figure 10 shows the spectral densities near the middle of the Brillouin zone ($q_{\parallel}=0.6k_{\bar{\Gamma}\bar{X}}$). Since various surface modes are excited in the impact scattering region, we show not only the perpendicular vibrations but also the parallel vibrations of the surface atoms. The Wallis mode (S_2) is strongly localized, because it is located at the middle of the gap between the bulk continua. The hybridization between S_2' and S_4 discussed above can be also seen; at the higher-energy part, the parallel vibration of the first-layer carbon mixes with the perpendicular vibration of the second-layer carbon. Concerning the acoustical part, there appears a sharp peak caused by the Rayleigh mode S_1 and a relatively broad peak by the longitudinal mode S_6. One can see that these local spec-

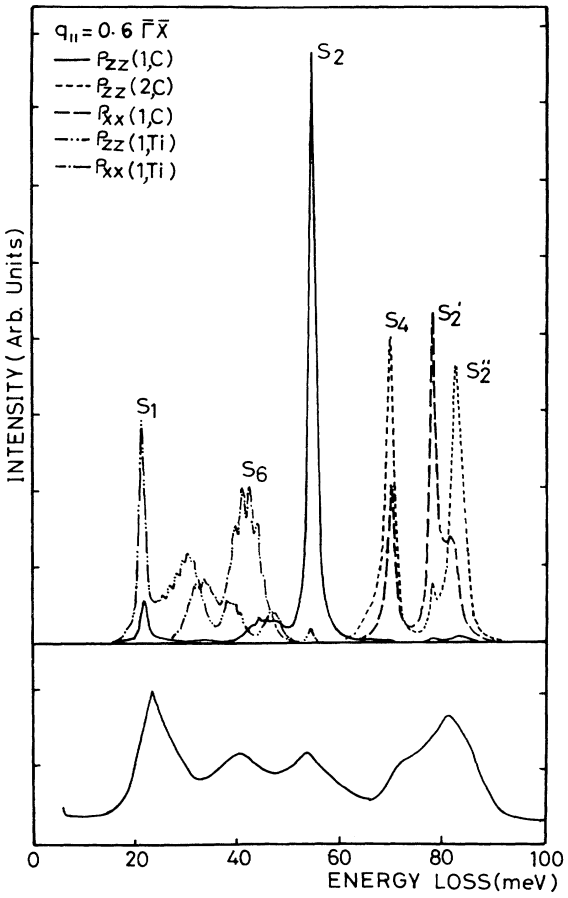

FIG. 10. Local spectral density of the relaxed surface at the wave vector of $q_{\parallel}=0.6k_{\bar{\Gamma}\bar{X}}$, and the corresponding EELS spectrum (lower part). The hybridization of the two modes (S_2' and S_4) are observed. The S_2 (Wallis) mode is strongly localized because it drops down to the middle point of the energy gap of the two bulk-phonon continua.

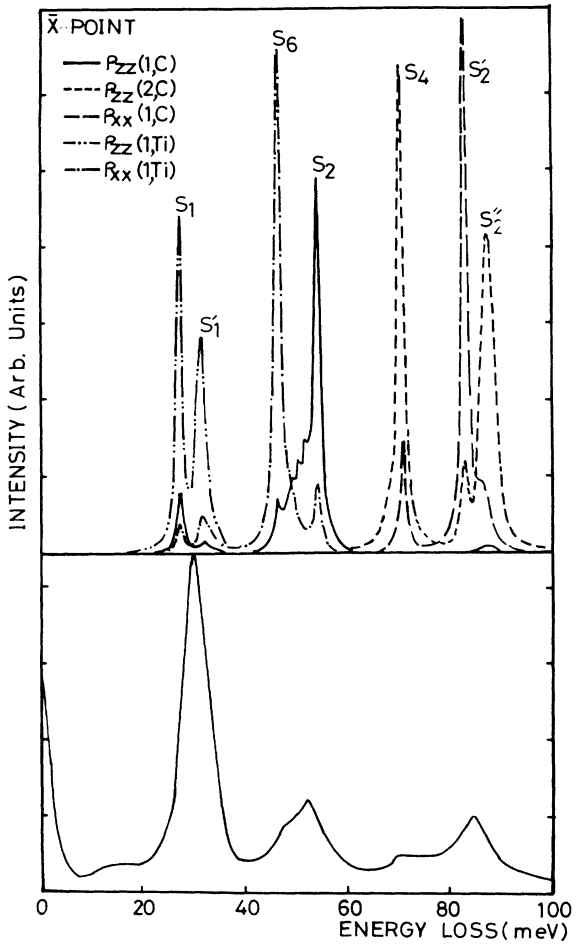

FIG. 11. Local spectral densities of the relaxed surface at the $\bar{X}$ point and the corresponding EELS spectrum (lower part). The S_6 (LA) mode is also highly localized because it falls into a gap within the acoustical bands.

tral densities explain fairly well the EELS spectrum shown in the lower part of Fig. 10.

At the $\bar{X}$ point, as shown in Fig. 11, S_6 becomes the highly localized mode at the first-layer Ti atom, because it drops down to the gap within the bulk acoustical continuum as discussed in Fig. 8. The S_1, S_2, S_4, and S_2' peaks are also localized. In the S_2' and S_4 modes, however, some features of the hybridization remain even at the $\bar{X}$ point. Additionally, two new peaks appear; one is just above the Rayleigh mode denoted by S_1', and the other mode (S_2'') appears above the S_2' mode. The S_1' mode is the quasiperpendicular motion of the second-layer Ti atoms. The experimental peak of the Rayleigh mode appears between those two lowest peaks (S_1 and S_1'). Another peak denoted by S_2'' is the high-energy mode, in which the second-layer carbon mainly vibrates in the perpendicular direction. The observed experimental peak is also located between the two highest-energy peaks. These new modes originate from the stiffening of the stretching force constant between the first and second layers, which are introduced in this model.

C. Surface relaxation

It has been known from LEED experiments on some transition-metal surfaces that the thermal vibrational amplitudes near the surfaces are larger than those in the bulk.[26] In the case of TiC(100), it is true for the vibration of the first-layer atoms, but not for the perpendicular vibration of the second-layer carbon as exemplified by the existence of the S_2' mode. The origin of S_2' is the stiffening of the stretching force constant between the first-layer Ti and the second-layer carbon. This phenomenon cannot be explained by changing the other parameters in this shell model.

This stiffening strongly suggests the atomic and/or electronic relaxation near the surface. Moreover, the *ab initio* calculation of the electronic structure of the "ideal TiC(100) surface" (all surface atoms in their ideal bulk positions) has also suggested that a rumpling structure occurs on the "real surface."[27] Additionally, similar bulk-above surface modes due to the atomic relaxation are discussed theoretically for the alkali halides;[8,9] how-

ever, the character of the surface mode is different from the S_2' mode. At present, no experimental evidence for atomic relaxation has so far been detected on the TiC(100) surface within the experimental accuracy of ion scattering ± 0.1 A.[21]

The additional changes in the force constants in Table I are not the unique solution for the explanation of the experimental dispersion curves. For instance, the energy bandwidth of the S_2 dispersion curves can be changed by changing the Coulomb terms instead of the parameter change of $C(11)$ in Table I,[7] and the vibrational energy of the Rayleigh mode S_1 can be increased at the zone boundaries by changing the polarization effect.[28] If we change these Coulomb terms, however, we must rearrange also the short-range parameters in order to compensate the vibrational-energy shift due to the change in Coulomb terms.[7] Therefore advanced theoretical works including *ab initio* dynamical calculations and precise experimental investigations of the surface structure are required to clarify the surface atomic and/or electronic relaxation on the TiC(100) surface.

---

*Permanent address: Institut für Grenzflächenforschung und Vakuumphysik (IGV) der Kernforschungsanlage (KFA) Jülich, Postfach 1913, D-5170 Jülich, West Germany.

[1]R. F. Wallis, Phys. Rev. **105**, 540 (1957).

[2]R. F. Wallis, D. L. Mills, and A. A. Maradudin, in *Localized Excitation in Solids,* edited by R. F. Wallis (Plenum, New York, 1968), p. 403.

[3]A. A. Lucas, J. Chem. Phys. **48**, 3156 (1968).

[4]S. Y. Tong and A. A. Maradudin, Phys. Rev. **181**, 1318 (1969).

[5]For example, T. Chen, G. P. Alldrege, F. W. deWette, and R. E. Allen, Phys. Rev. Lett. **26**, 1543 (1971).

[6]G. Benedek, M. Miura, W. Kress, and H. Bilz, Phys. Rev. Lett. **52**, 1907 (1984).

[7]H. Ishida and K. Terakura, Phys. Rev. B **34**, 5719 (1986).

[8]F. W. deWette, W. Kress, and U. Schroder, Phys. Rev. B **32**, 4143 (1985).

[9]W. Kress, F. W. deWette, A. D. Kulkarni, and U. Schroder, Phys. Rev. B **35**, 5783 (1987).

[10]G. Brusdeylins, R. B. Doak, and J. P. Toennis, Phys. Rev. Lett. **44**, 1417 (1980).

[11]C. Oshima, R. Souda, M. Aono, S. Otani, and Y. Ishizawa, Phys. Rev. B **30**, 5361 (1984).

[12]C. Oshima, R. Souda, M. Aono, S. Otani, and Y. Ishizawa, Phys. Rev. Lett. **56**, 240 (1986).

[13]C. Oshima, R. Souda, M. Aono, S. Otani, and Y. Ishizawa, Solid State Commun. **57**, 283 (1986).

[14]C. Oshima, R. Souda, M. Aono, S. Otani, and Y. Ishizawa, Surf. Sci. **178**, 519 (1986).

[15]G. Brusdeylins, R. Rechsteiner, J. G. Skofronick, and J. P. Toennis, Phys. Rev. Lett. **54**, 466 (1985).

[16]L. Pintschvious, W. Reichardt, and B. Scheerer, J. Phys. C **11**, 1557 (1978).

[17]C. Oshima, M. Aono, T. Tanaka, S. Kawai, S. Zaima, and Y. Shibata, Surf. Sci. **102**, 312 (1981).

[18]M. Aono, Y. Hou, R. Souda, C. Oshima, S. Otani, and Y. Ishizawa, Phys. Rev. Lett. **50**, 1293 (1983).

[19]F. Gompf and W. Reichardt, Report No. 2538, 1977 (unpublished).

[20]W. Weber, Phys. Rev. B **8**, 5082 (1973).

[21]M. Aono and R. Souda, Jpn. J. Appl. Phys. **24**, 1249 (1985).

[22]For instance, L. Rayleigh, *Theory of Sound* (Dover, New York, 1945), Vol. I.

[23]H. Ibach and D. L. Mills, *Electron Energy Loss Spectroscopy and Surface Vibrations* (Academic, New York, 1982).

[24]R. Franchy, C. Oshima, T. Aizawa, R. Souda, S. Otani, and Y. Ishizawa (unpublished).

[25]M. Wuttig, C. Oshima, T. Aizawa, R. Souda, S. Otani, and Y. Ishizawa (unpublished).

[26]A. U. MacRae, Surf. Sci. **2**, 522 (1964).

[27]E. Wimmer, A. Neckel, and A. J. Freeman, Phys. Rev. B **31**, 2370 (1985).

[28]G. Benedek, G. P. Brivio, L. Miglio, and V. R. Velasco, Phys. Rev. B **26**, 497 (1982).